IVYSPRING INTERNATIONAL PUBLISHER

Theranostics

2017; 7(17): 4149-4167. doi: 10.7150/thno.21040

Research Paper

# Dual-targeting Theranostic System with Mimicking Apoptosis to Promote Myocardial Infarction Repair *via* Modulation of Macrophages

Jingli Chen[1, 2*], Jun Yang[1*], Ruiyuan Liu[1], Chenmeng Qiao[1], Zhiguo Lu[1], Yuanjie Shi[1], Zhanming Fan[3]✉, Zhenzhong Zhang[2]✉, Xin Zhang[1] ✉

1. State Key Laboratory of Biochemical Engineering, Institute of Process Engineering, Chinese Academy of Sciences, Beijing 100190, PR China;
2. School of Pharmaceutical Sciences, Zhengzhou University, Zhengzhou 450001, PR China;
3. Department of Radiology, Beijing An Zhen Hospital, Capital Medical University, Beijing Institute of Heart, Lung and Blood Vessel Disease, Beijing 100029, PR China.

* These authors contributed equally to this work.

✉ Corresponding authors: Xin Zhang, State Key Laboratory of Biochemical Engineering, Institute of Process Engineering, Chinese Academy of Sciences. Tel./fax: +86 10 82544853. Email: xzhang@ipe.ac.cn. Zhenzhong Zhang, School of Pharmaceutical Sciences, Zhengzhou University. Tel.: +86 371 67781910; fax: +86 371 67781908. Email: zhangzz08@126.com. Zhanming Fan, Department of Radiology, Beijing An Zhen Hospital, Capital Medical University, Beijing Institute of Heart, Lung and Blood Vessel Disease. Tel.: +86 10 64456310; fax: +86 10 64456310. Email: fanzm120@126.com.



Received: 2017.05.16; Accepted: 2017.07.17; Published: 2017.09.26

## Abstract

Currently unsatisfactory treatment of myocardial infarction (MI) is due to the unbridled inflammation and the delayed diagnosis at the early stage. To address these problems, firstly, phosphatidylserine (PS) was used to modulate the phenotypes of macrophages (MΦ) and resolve the early inflammation *via* binding to PS receptors (PSR) on macrophage surface. Secondly, highly-sensitive magnetic iron oxide nanocubes (MIONs) were adopted to realize the early visualization *via* magnetic resonance imaging (MRI). However, the major drawback for MIONs as contrast agents was their hydrophobic properties and insufficient delivery. Hence, zwitterionic biodegradable copolymer poly(lactide)-polycarboxybetaine (PLA-PCB, PP), companied with PS, was used to provide a good colloidal stability and long blood circulation for the nanocubes. Given the above, a theranostic nanosystem (PP/PS@MIONs) was constructed for early treatment of MI. With external magnetic field-induced targeting and PS targeting, the nanosystem enhanced the accumulation in infarcted area, and accelerated the resolution of early inflammatory responses. Moreover, the nanocubes in system were promoted to escape from endosomes/lysosomes *via* protonation of PCB, which contributes to accurate MRI. This nanosystem showed good inflammation-resolving effects and imaging ability in MI model rats. Therefore, this theranostic nanosystem can realize accurate visualization and significantly improve the treatment efficacy of MI at early stage.

Key words: myocardial infarction, theranostic system, inflammation regulation, mimicking apoptosis, magnetic resonance imaging.

## Introduction

Myocardial infarction (MI) has become one of the leading causes of human morbidity and mortality [1]. During the early stage of MI, an intense inflammatory response is triggered as a defense mechanism. However, the excessive inflammation companied with up-regulated pro-inflammatory cytokines can enhance the myocardial injury and contribute to adverse remodeling and heart failure (HF) [2-7]. Currently, the clinic treatments of MI only aim to alleviate the symptoms and do not resolve the inflammation [8, 9]. Moreover, imaging is critical for early diagnosis of MI. Recently, magnetic resonance imaging (MRI) enhanced by traditional gadolinium contrast agents like diethylenetriaminepentaacetic

acid gadolinium (III) (Gd-DTPA) is commonly used to assess MI. But these contrast agents have short half-life, low relaxivity and potential renal risks. More importantly, the gadolinium-based small molecular contrast agents only distribute extracellularly, which fail in MRI of specific area of MI [10, 11]. These limitations of therapy and inaccurate diagnosis hinder the efficient treatment of MI.

Hence, new strategies to address the resolution of initial inflammation and accurate assessment at early stage are eagerly needed for MI treatment [4, 12-17]. Karin Montet-Abou *et al.* used [$^{44}$AANA$^{47}$]-RANTES, a potent anti-CCL5 agent, as an anti-inflammatory treatment of MI in Sprague-Dawley rats [18]. This treatment reduced the inflammatory injury and preserved the cardiac function. Besides, it was well known that iron oxide nanoparticles could be endocytosed by the monocytes/macrophages [7, 11, 19, 20]. Herein, superparamagnetic iron oxide nanoparticles (SPIONs) were used in this treatment to load into monocytes/macrophages to detect the infarct size *via* enhanced MRI. But this strategy still exhibited some shortages. Firstly, the anti-inflammatory agent had low efficiency of retention in infarcted area without specific targeting delivery, which led to an unsatisfactory therapy effect. Secondly, though SPIONs in this system were endocytosed by macrophages for MRI, the contrast agents had low relaxivity and couldn't effectively release into cytoplasm, which impacted the image resolution and clarity.

In our study, to overcome these problems, a dual-targeting theranostic system with mimicking apoptosis was designed (PP/PS@MIONs). It is well known that the endocytosis of apoptotic cells by macrophages can elicit an anti-inflammatory response and promote the pro-inflammatory macrophages (M1) differentiate to a reparative phenotype (M2) [21-26]. The endocytosis is explained by the externalized phosphatidylserine (PS) on membranes of apoptotic cells specifically binding to the PS receptors (PSR) on macrophages surface [27-29]. Inspired by this, PS was presented in our nanosystem to suppress the inflammation by mimicking the apoptotic cells and regulate the phenotypes of macrophages. Moreover, magnetic iron oxide nanocubes (MIONs) with extremely high magnetic sensitivity were used to enhance the retention of PS *via* magnetic targeting and improve the resolution of MRI. However, these obtained MIONs by thermal decomposition method are extremely hydrophobic [30]. With short hydrophilic head, PS could not keep the MIONs stable for *in vivo* application and generate sufficient release. Considering this, a zwitterionic polymer PCB was used. The polycarboxybetaine (PCB)-based amphiphilic block polymer could improve the hydrophilicity of hydrophobic drugs and the controlled release in target sites in our previous work [31]. Hence, a zwitterionic biodegradable copolymer poly(lactide)-polycarboxybetaine (PLA-PCB, PP), companied with PS, was adopted in our theranostic nanosystem (PP/PS@MIONs) (Figure 1A).

As illustrated in Figure 1B, PP/PS@MIONs were administrated intravenously with a magnetic field outside the infarcted area. The accumulation and retention of PP/PS@MIONs were enhanced by magnetic induction and PS targeting to macrophages in infarcted tissue. (1) The bind of PSR by PS activated the inflammatory macrophages (M1) to convert to a pro-resolving phenotype (M2). (2) M2 macrophages could induce an anti-inflammatory response with up-regulation of transforming growth factor β1 (TGF-β1), interleukin-10 (IL-10) and inhibition of pro-inflammatory cytokines like tumor growth factor α (TNF-α) and so on. The modulation of macrophages and the increased secretion of anti-inflammatory local regulators in the cardiac microenvironment promoted resolution of inflammation and improved the MI healing. On the other hand, after PS binding to PSR on macrophages, (1') PP/PS@MIONs were endocytosed into endosomes/lysosomes with an acid environment. (2') Then PCB was protonated and helped the endosomal/lysosomal escape of PP/PS@MIONs. (3') After that, MIONs were released into the cytoplasm for the enhanced MRI. Thus, this theranostic nanosystem (PP/PS@MIONs) was hypothesized to realize accurate visualization and significantly improve the treatment efficacy of MI at early stage.

## Materials and methods

### Materials

L-Lactide (LLA, 99%), stannous 2-ethylhexanoate ($Sn(Oct)_2$, 95%), β-propiolactone (98%), 2-bromo-2-methylpropionyl bromide, 2-(N, N'-dimethylamino) ethyl methacrylate (DMAEMA, 98%), copper bromide (98%), 2-hydroxylethyl 2-bromoisobutyrate (HEBIB, 95%) and fluorescamine (FA, 98%) were obtained from J&K Scientific Ltd (Shanghai, China). N, N, N', N', N''-pentamethyldiethylenetriamine (PMDETA, 99%), potassium carbonate, sodium chloride, 3-(4, 5-dimethylthiazol-2-yl)-2, 5-diphenyltetrazoplium bromide (MTT) and Escherichia coli lipopolysaccharide (LPS) were purchased from Sigma-Aldrich (St. Louis, Missouri, USA). Iron (III) acetylacetonate (99%), oleic acid (90%), benzyl ether (99%) and 4-biphenylcarboxylic acid (99%) were purchased from Alfa Aesar. L-α-phosphatidylserine

(99%) were purchased from Aladdin (Shanghai, China). Dulbecco's Modified Eagle Medium (DMEM) and fetal bovine serum (FBS), L-glutamine, penicillin (10,000 U/mL), streptomycin (10 mg/mL) and trypsin-EDTA were purchased from Invitrogen (Carlsbad, CA, USA). All ELISA kits (mouse TGF-beta1 platinum ELISA, mouse TNF-alpha platinum ELISA, mouse IL-1beta platinum ELISA, and mouse IL-10 platinum ELISA) and antibodies (*F4/80,* CD86) used for Fluorescence Activated Cell Sorting (FACS) were purchased from eBioscience (CA, USA). Antibody (CD206) were purchased from Biolegend (CA, USA). Antibodies (mannan binding lectin, *alpha* smooth muscle actin (α-SMA)) used for immunohistochemistry were purchased from Abcam (Cambridge, UK). Thioglycollate medium was purchased from Becton, Dickinson and Company (MD21152-0999, USA). Cy7 and Prussian blue staining kit were obtained from Solarbio Science & Technology Co., Ltd (Beijing, China). All the reagents were of analytical grade and used without further purification. High-purity water (Milli-Q Integral) with a conductivity of 18 MΩ $cm^{-1}$ was used for the preparation of all aqueous solutions.

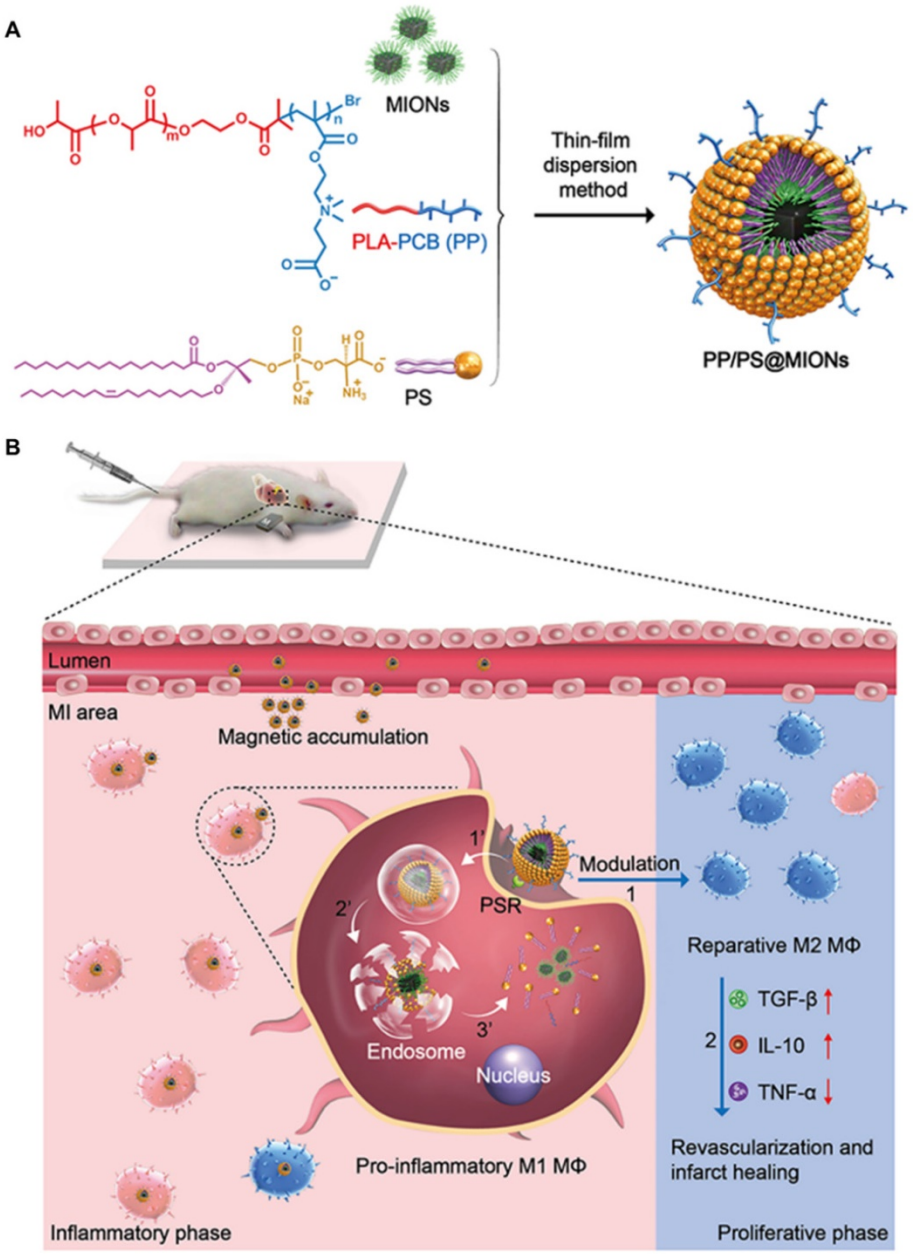


**Figure 1. Preparation of the nanotheranostic system (PP/PS@MIONs) and the function of inflammatory regulation and MI repair.** (**A**) Chemical structural formula for each components and formation of the theranostic system (PP/PS@MIONs) *via* the thin-film dispersion method. (**B**) Schematic diagram of cellular uptake, subcellular release of MIONs and activation of M1 macrophages by PP/PS@MIONs with an external magnetic field outside the infarcted area. PP/PS@MIONs accumulated in MI area due to magnetic targeting and PS targeting. (1) M1 macrophages were activated to M2 phenotype by the interactions between PS and PSR. (2) M2 macrophages up-regulated the secretion of TGF-β1 and IL-10 and inhibited that of TNF-α, which promoted revascularization and infarct healing. Simultaneously, (1') PP/PS@MIONs were endocytosed. (2') Protonation of PCB in endosomes/lysosomes. (3') MIONs escaped and released into cytoplasm for MRI. M: magnet.

### Synthesis of carboxybetaine (CB) monomer

Synthesis of CB was performed according to the previous report [31, 32]. Briefly, β-propiolactone (0.43 g, 6 mmol), DMAEMA (0.79 g, 5 mmol) and 5 mL of dried dichloromethane was added into a glass tube flame-dried three times before use, and followed by degassing in three freeze/pump/thaw cycles. The tube was sealed and stirred at 0 °C for 7 h. The white precipitate was washed with 50 mL of dried dichloromethane and 50 mL of anhydrous acetone. The product was then dried under reduced pressure to obtain the final CB. CB: $^1$HNMR (600 MHz, $D_2O$): δ=6.06: (-C**H**=$CCH_3$-), δ=5.85: (-C**H**=$CCH_3$-), δ=4.58: (-OC**H**$_2$$CH_2$N-), δ=3.70: (-$OCH_2$C**H**$_2$N-), δ=3.59: (-NC**H**$_2$$CH_2$COO-), δ=3.10: (-NC**H**$_3$C**H**$_3$-), δ=2.64: (-$NCH_2$C**H**$_2$COO-), δ=1.84: ($CH_2$=CC**H**$_3$-).

### Synthesis of $PLA_n$-Br Macroinitiators

Ring-opening polymerization (ROP) of L-lactide (LLA) promoted by initiator and catalyst was widely adopted [33]. Here the initiator HEBIB (0.345 mmol), LLA (6.95 mmol) and $Sn(Oct)_2$ (0.1 wt.-% of the monomer) were added into a dried glass tube with 4 mL dried toluene inside, followed with degassing in three freeze/pump/thaw cycles. The tube was sealed and stirred at 100 °C for overnight. The product was dissolved in chloroform and precipitate in the absence of an excess of diethyl ether. Then after washed with cold methanol at least for three times, the last product was dried under reduced pressure to obtain the final $PLA_n$-Br. $PLA_n$-Br: $^1$HNMR (600 MHz, $CDCl_3$): δ=1.57: (-COCHC**H**$_3$-), δ=1.93: (C**H**$_3$ C**H**$_3$CBr-), δ=5.17: (-COC**H**$CH_3$-).

### Synthesis of PLA-PCB polymer

PLA-PCB was synthesized using an atom transfer radical polymerization (ATRP) [31]. $PLA_n$-Br (0.144 g, 0.025 mmol), CuBr (7.2 mg, 0.05 mmol), PMDETA (10.4 μL, 0.05 mmol), CB (229 mg, 1 mmol) and 5 mL methanol were added into a clean and dry flask. The flask was degassed in three freeze/pump/thaw cycles and recharged with nitrogen. The flask was sealed and stirred at 60 °C for 24 h. The impurities and unreacted molecules were removed by sequentially dialyzing in a Cellu SepH1-membrane (MWCO 3,500) against ethanol and deionized water for 48 h respectively and freeze-dried to obtain the final product. PLA-PCB: $^1$H NMR (600 MHz, $CDCl_3$): δ=5.17: (-COC**H**$CH_3$-), δ=4.10: (-OC**H**$_2$$CH_2$N-), δ=3.0-4.8: (-$OCH_2$C**H**$_2$NC**H**$_2$$CH_2$-), δ=2.60: (-$NCH_2$C**H**$_2$COO-), δ=2.25: (-NC**H**$_3$C**H**$_3$-), δ=1.80: (-C**H**$_2$=$CCH_3$-), δ=1.57: (-COCHC**H**$_3$-), δ=1.28: (-$BrCH_2CC$**H**$_3$-).

### Synthesis of MIONs

MIONs was synthesized by high temperature thermal decomposition method [30]. A mixture of $Fe(acac)_3$ (iron (III) acetylacetonate, 0.706 g), oleic acid (1.1 g), 4-biphenylcarboxylic acid (0.4 g) and benzylether (10 mL) were added into a three-neck flask and dried under vacuum for 40 min at 120 °C. Then the solution was heated to 290 °C at a rate of 20 °C/min for 30 min in the absence of vigorous magnetic stirring. The solution was cooled down to room temperature and washed with methanol for times. Finally, the nanocubes were dissolved in chloroform.

### Preparation of PP/PS@MIONs

The preparation of PP/PS@MIONs as an example was described as follows. In brief, PLA-PCB and PS at a molar ratio of 1: 10 were dissolved in chloroform with MIONs. The organic phase was removed at 55 °C on a rotary evaporator to obtain a thin lipid film which would be hydrated with phosphate buffer saline (PBS) and underwent a sonication at 37 °C for 30 min. The nanoparticles (NPs) were washed with repeated ultracentrifugation (2,500 rpm for 30 min at room temperature) for three times to remove excess materials. Finally the pellets were resuspended at a PS concentration of 3 mM and Fe concentration of 1 mg/mL.

### Characterization of PP/PS@MIONs

A dynamic light scatting (DLS) instrument and a Zetasizer Nano ZS instrument (Malvern Instruments) were used to detect the diameters and the surface zeta potentials of the NPs, respectively. Transmission electron microscopy (TEM) images were taken on TEM (JEM-2100 electron microscope) at 200 kV. The concentrations of Fe and P of the NPs were determined by the inductively coupled cytoplasm mass spectrometer (ICP-MS) by using ICAP-QC (Thermo, USA).

### Magnetic properties of PP/PS@MIONs

*M-H* curves were obtained by superconducting quantum interference device (SQUID) (Quantum Design, USA). The $r_2$ value was calculated as by measuring the change in the spin-spin relaxation rate ($R_2$) per unit iron concentration. $R_2$ was calculated as $1/T_2$. $T_2$ values of nanoparticles were measured by using a 3.0 T MRI scanner (Verio, Siemens Healthcare, Erlangen, Germany): TR = 5000 ms, TE = 21, 43, 64, 85, 107, 128, 150, 171, 192 ms. Turbo spin echo $T_2$-weghted MR images of the phantom were acquired by using the following parameters: flip angle = 150, ETL = 18, TR = 5000 ms, TE = 85 ms, field of view FOV = 200 × 250 $mm^2$, matrix = 245 × 384, slice thickness = 3 mm,

Number of Averages = 1.

### PH-sensible proton sponge mechanism of PLA-PCB

The buffering capacity of PLA-PCB was measured by acid-base titration. Briefly, PLA-PCB were dispersed in 0.01 M NaCl. Then 1 M NaOH was used to adjust the solution to pH 10. Add 0.1 M HCl stepwise to the solution to obtain the titration profile. To measure the pH-sensibility of PCB modified NPs, NPs were incubated in PBS of different pH values at 37 °C for 30 min. the zeta potential of the NPs was measured by using a Zetasizer Nano ZS instrument.

### Cell culture

RAW264.7 macrophages from Chinese Academy of Medical Sciences were cultured at 37 °C under a humidified atmosphere of 5% $CO_2$ in DMEM supplemented with 10% FBS, 2 mM L-glutamate, 100 U/mL penicillin and 100 μg/mL streptomycin.

Primary peritoneal macrophages were isolated from Balb/c mice as described previously [34, 35]. Six to eight week-old female Balb/c mice were purchased from the Academy of Military Medical Sciences of China. All procedures involving experimental animals were performed in accordance with protocols approved by the institutional Animal Care and Use Committee of Peking University. Following injection of 1 mL thioglycollate medium into the peritoneum continuously for 3 days, the animals were sacrificed on day 4. Then 5 mL of DMEM supplemented with 1% (v/v) penicillin/streptomycin and 5% (v/v) FBS was injected into the peritoneum. After massaging the abdomen gently, the cell lavage was collected. The peritoneum lavage underwent a centrifugation (1,000 rpm for 3 min at room temperature) and was maintained in ACK buffer for 2 min for lysing the erythrocytes. The remaining cells were resuspended in medium (DMEM containing 1% L-glutamine, 1% penicillin-streptomycin solution, 10% FBS) and $1\times10^6$ cells were then seeded into 24-well plates incubated at 37 °C under 5% $CO_2$ atmosphere. On day 5, 1 mL/well fresh complete DMEM were added after removing the existed culture medium to select for the adherent macrophages.

### Cytotoxicity assay

*In vitro* cytotoxicity of PP/PS@MIONs was assessed by an MTT colorimetric assay with RAW264.7 macrophages. $1\times10^4$ cells/well in 100 μL complete DMEM were seeded onto a 96-well culture plate to attach overnight. The existed culture medium was replaced with 100 μL fresh complete DMEM in the presence of different formulations. After 24 h incubation, 20 μL/well of MTT solution (5 mg/mL in PBS) was added and incubated at 37 °C in 5% $CO_2$ for 4 h. Then aspirated the solution in the well gently and added 200 μL/well of DMSO to each well to dissolve the formazan crystal. The absorbance was measured at 570 nm with a microplate reader (Tecan, Switzerland). The percentage of cell viability was determined by comparing cells treated with different formulations to the untreated control cells. The percent relative cell viability was calculated according to the following equation:

$$\text{Cell viability (\%)} = OD_{sample}/OD_{control} \times 100\%$$

### Cellular uptake *in vitro*

The uptake of the NPs by RAW264.7 macrophages was performed as follows. $1\times10^6$ cells were treated with Cy7 labeled NPs (100 μL/million cells) for different time. After being washed, cells were harvested and examined by FACS analysis. The excitation and emission of Cy7 were 747 nm and 774 nm, respectively.

### Confocal laser scanning microscope measurement

The endosomal/lysosomal escape was investigated by using confocal laser scanning microscope (CLSM, Zeiss Co., Germany). Briefly, $4\times10^5$ RAW264.7 macrophages were seeded into Petri dishes to attach overnight. The existed culture medium was replaced with 500 μL fresh complete DMEM containing different formulations including PBS, free fluorescamine (FA) labeled PS and PP/PS@MIONs prepared with FA labeled PS. The concentration of PS was 0.3 μmol/million cells. After the macrophages were incubated at 37 °C for 4 h and 12 h respectively, the cells were washed three times with PBS followed by staining with Lysotracker Red at 37 °C for 40 min. Then the cells were washed three times again with PBS and fixed with 4% paraformaldehyde for 15 min at room temperature. The excitation and emission of Lysotracker Red were 577 nm and 590 nm, respectively. The excitation and emission of FA labeled PS were 390 nm and 475 nm, respectively. The co-localization ratio of the fluorescence intensity of various formulations was calculated by Zen Co-localization software with 8 random fields of view.

### *In vitro* activation of peritoneal macrophages and cytokines secretion

For anti-inflammation studies, peritoneal macrophages, an accessible cell type compared to cardiac macrophages, were treated with different formulations. The groups were set as cells with no treatment (NT), cells treated with LPS following PBS (control), cells treated with LPS following PP@MIONs (PP@MIONs), cells treated with LPS following free PS

(Free-PS) and cells treated with LPS following PP/PS@MIONs (PP/PS@MIONs). The concentration of PS was 0.3 μmol/million cells. Firstly, we co-incubated cells with LPS (1 μg/mL) for 24 h at 37 °C. Then formulations and cells were co-cultured for 12 h, the supernatant was collected and the cells were washed with flow buffer. Then the cells were stained with anti-mouse F4/80 antigen eFluor® 450 for the total macrophages, anti-mouse CD86 (B7-2) APC for pro-inflammation macrophages and PE anti-mouse CD206 (MMR) for reparative macrophages, respectively. After being washed and repeated centrifugation (1,000 rpm for 3 min at room temperature) twice with PBS, the cells were resuspended in cell staining buffer examined by FACS.

The cytokines secretion of TNF-α, TGF-β1, IL-1β and IL-10 in the supernatant was assayed by the respective enzyme-linked immunosorbent assay (ELISA). The absorbance at 450 nm (with 620 nm as reference) was measured by an Infinite M200 Microplate Spectrophotometer (Tecan, Männedorf, Switzerland).

### Blood pharmacokinetics

To determine the blood pharmacokinetics *in vivo*, KM mice were randomly divided (n=3). Fluorescamine (FA) was used to label PS as in aforementioned confocal laser scanning microscope measurement section, and Cy7 was chosen to label the nanoparticles as in above-mentioned cellular uptake *in vitro* section. The mice were injected intravenously through the tail vein with PS, PP@MIONs and PP/PS@MIONs, respectively, at the equivalent dose of 10 mg/kg Fe and 30 μmol/kg PS. Approximately 100 μL of blood sample was collected in a heparinized tube from the orbital venous plexus at 5 min, 0.5 h, 1 h, 2 h, 4 h, 8 h, 12 h and 24 h post injection. The plasma was centrifuged and measured by fluorescence spectrophotometry. The plasma half-time ($t_{1/2}$) was calculated by the non-compartment pharmacokinetic model.

### Induction of MI and NPs injection

Lewis rats were used to conduct a randomized and blinded study. One group (n=8-11) was given a sham surgery while other four groups (n=8-11) underwent MI *via* permanent ligation of the left descending artery [17]. The animal studies were performed in accordance with the institutional ethics committee regulations and guidelines on animal welfare.

48 h after the MI surgery, rats were anesthetized by inhalation of oxygen mixed with 1.5% isoflurane, and were injected *i.v.* with different formulations before the examination of cardiac function. The groups were set as rats received a sham surgery (sham), MI rats treated with saline (saline), MI rats treated with PP@MIONs (PP@MIONs), MI rats treated with free PS (Free-PS), MI rats treated with PP/PS@MIONs (PP/PS@MIONs) and MI rats treated with PP/PS@MIONs exposed to an external magnetic field (PP/PS@MIONs + M). The external magnetic field was constructed as a 0.4-T neodymium permanent magnet (M) placing outside the heart for 1 h. Take a 250 g rat as an example, 2.5 mg of Fe and 7.5 μmol of PS were injected to the caudal vein.

### *In vivo* MRI and cardiac function analysis

MRI of MI rats were performed under a 7.0 T MRI scanner to examine cardiac function. After anesthetization by inhalation of oxygen mixed with 1.5% isoflurane, localizer scans were performed to identify the short axis of the left ventricle (LV). Before the NPs injection, cine sequence at several short-axis locations was used to examine cardiac function of the hearts 48 h post-MI surgery to perform baseline measurements, and again at 1 month post-injection (32 days post-MI). The parameters of cine were as the following: field of view 60×60 mm, slice 1 mm, matrix 192×192 pixels, flip angle 20 degrees, 12 frames per RR interval, TR=157.4 ms, TE=2.38 ms, 4 averages.

For left ventricle end systolic and left ventricle diastolic volume (LESV and LEDV) determinations, the endocardial border was identified with ImageJ and volumes calculated as follows [36]:

$$\text{LV volume} = \sum_{i=1}^{\text{all slices}} (\text{endocardial area}) \times (\text{slice thickness})$$

And then ejection fraction (EF) could be calculated as follows:

$$EF = (LEDV\text{-}ESV)/EDV \times 100\%$$

To examine myocardial area, MRI of MI rats were performed under a 7.0 T MRI scanner. After anesthetization and identification of the short axis of the LV, $T_2$* imaging was performed 24 h after NPs injection (72 h after MI surgery). Four groups were detected including MI rats treated with saline (saline), MI rats treated with PP@MIONs (PP@MIONs), MI rats treated with PP/PS@MIONs (PP/PS@MIONs) and MI rats treated with PP/PS@MIONs exposed to an external magnetic field (PP/PS@MIONs + M). The external magnetic field was constructed as a 0.4-T neodymium permanent magnet (M) placing outside the heart for 1 h. The parameters were as follows: field of view 60×60 mm; slice thickness 1 mm; TR=56.32 ms; TE=2.83 ms; matrix 192×192 pixels. After imaging, the hearts were harvested for Prussian blue staining.

### Laser speckle contrast analysis (LASCA) of infarcted tissues

1 month after the injection, following the examination of cardiac function, flow velocity and spatial vascular profile in the infarcted area were evaluated by laser speckle contrast imaging by using a MOORFLPI2 real-time blood flow zoom laser speckle imaging system (Moor Instruments, Ltd., UK).

### Immunohistochemical and morphometric analysis

After LASCA, the animals were euthanized, followed by heart perfusion with 60 mL cold saline. The hearts were harvested and fixed in 10% formalin, embedded in paraffin, and sectioned into 3 transverse slices and each slice was sectioned into 4 μm thickness. These cross-sections were stained with Masson's trichrome for nuclei, cytoplasm, and collagen to visualize the infarct. Interstitial fibrosis was measured in non-infarcted septal wall regions, while infarct fibrosis percentage was determined in the infarct region. Four parameters including average scar thickness (mm), average wall thickness (mm) (averaged from at least three measurements of septum thickness), LV cavity area ($mm^2$), and whole LV area ($mm^2$) were identified with ImageJ and calculated as follows [37]:

$$\text{Relative scar thickness} = \text{average scar thickness}/\text{average wall thickness}$$

$$\text{Expansion index} = (\text{LV cavity area}/\text{whole LV area})/\text{relative scar thickness}$$

Finally, the organs of different formulations, including the heart, liver, spleen, lung and kidney, were harvested for Prussian blue staining 1 month after the treatment. The magnification was 200×.

### Iron concentration assay *in vivo*

1 d and 1 month after the intravenous administration, the rats were euthanized. The tissues, including heart, liver, spleen, lung and kidney, were evaluated the concentration of iron by Iron Assay Kit (Sigma-Aldrich). The absorbance (OD) of the samples was tested at 593 nm.

### Statistical Analysis

All data were expressed as mean ± SD unless otherwise indicated. All experiments were done in triplicate with a minimum of three independent experiments. Statistical significance was analyzed by using one-way ANOVA. Statistical differences in behavioral data were determined by using two-way repeated measures ANOVA. Significance was accepted at $P < 0.05$.

## Results and Discussions

### Preparation and characterization of zwitterionic polymer PLA-PCB (PP)

PLA-PCB was prepared by combining ROP and ATRP (Figure 2). The structures of the monomer CB, macro-initiators $PLA_n$-Br and diblock copolymer PLA-PCB were confirmed by $^1H$ NMR spectra (Figure 3). In Figure 3B, peaks k and j were assigned to the methine and methyl protons on PLA backbone. The appearance of peak i came from the methyl protons on the initiator HEBIB. The block length of the PLA was calculated from the ratio of integrated intensities between the peaks k and i. Calculated from the spectra, the DPs of PLA was 20, 40 and 60. In Figure 3C, characteristic peaks c, d, f and h were assigned to the PCB block, indicating successful PLA-PCB diblock copolymer synthesis. The DP of PCB was fixed at 40 to evaluate the influence of length of PLA on the properties of the system.

### Characteristics of MIONs loaded NPs (PP/PS@MIONs)

The MIONs loaded NPs were synthesized *via* the thin-film dispersion method through evaporating a thin film of PP, PS and MIONs mixture and performing an ultrasonic treatment after rehydration (Figure 1A). As shown in Figure 4A, the sizes of $P_{40}P$/PS@MIONs and $P_{60}P$/PS@MIONs were around 50 nm and 80 nm, while the sizes of $P_{20}P$/PS@MIONs were more than 500 nm and unstable visually. The charges of the PP/PS@MIONs were electrically neutral, but the zeta potential was range from 11 mV to 16 mV without PS. Except $P_{20}P$/PS@MIONs, other two PP/PS@MIONs presented good water-solubility and colloidal stability in biological environment (Figure 4B). This might because $PLA_{20}$-PCB had a relatively shorter hydrophobic block, which had insufficient interaction with the ligands coating on MIONs. The weak combination led to a larger size and instability. By transmission electron microscope (TEM) analysis (Figure 4C and D), the MIONs and PP/PS@MIONs exhibited a nanocube shape.

To investigate the magnetic properties of the NPs, the magnetization curves and $r_2$ values were measured. As shown in Figure 4E, $P_{40}P$/PS@MIONs and $P_{60}P$/PS@MIONs had comparable saturation magnetization of 75 emu/g Fe and 73 emu/g Fe, respectively. The *M-H* curves showed no remnant magnetization and coercivity at room temperature, which was contribute to the stability of the NPs. The insert picture showed the rapid accumulation of $P_{40}P$/PS@MIONs onto the cuvette wall induced by the magnet, which indicated the sensitivity of the NPs to a magnetic field. Besides, the $r_2$ relaxivities and

images of the two kind of NPs were measured by using 3.0 T MRI scanner (Figure 4F and G). The $r_2$ values were calculated to be 376.5 $s^{-1}$ $mM^{-1}$ and 327.0 $s^{-1}$ $mM^{-1}$ for $P_{40}P$/PS@MIONs and $P_{60}P$/PS@MIONs, respectively. Both the two values were much higher than that of the commercial contrast agents such as Feridex. That was because Feridex was obtained by the co-precipitation method [38], whereas nanocubes used in our system were synthesized by thermal decomposition method. These nanocubes had narrow size distribution, high crystallinity and good magnetic performances. Moreover, the higher magnetic sensitivity motivated us to develop the applications of these nanocubes as an efficient contrast agent of MRI for MI *in vivo*. From the previous data, the $P_{40}P$/PS@MIONs showed better physiochemical and magnetic properties. Herein, $P_{40}P$/PS@MIONs was chosen for the following studies.

In our previous study, the charge-reversible zwitterionic PCB was reported to be nearly neutral and could resist the nonspecific protein absorption at pH 7.4 [39]. After internalization into endosomes/lysosomes with a low pH, the charge of PCB could change to positive due to protonation process, which contributed the endosomal/lysosomal escape for PCB based NPs. Herein, the sensitivity of $PLA_{40}$-PCB to acid environment was tested (Figure 4H). As the pH value changed from 7.4 to 5.5, PCB exhibited a good buffering capacity in NaCl aqueous solution. The zeta potential of PCB-based $P_{40}P$/PS@MIONs was also measured in different acid conditions. Along with the decreasing pH value, the zeta potential of $P_{40}P$/PS@MIONs ascended from 4.3 mV to 22.0 mV, which confirmed the protonation of PCB (Figure 4I).

### *In vitro* cytotoxicity

RAW264.7 macrophages were used to test the biocompatibility of the theranostic system (PP/PS@MIONs) by using a methyl thiazolyl tetrazolium (MTT) assay. As illustrated in Figure 5A, PP/PS@MIONs had no effect on cell viability up to a concentration of 0.40 mg Fe/mL (with PS 1.5 mM), demonstrating the high biocompatibility of PP/PS@MIONs. However, PP@MIONs displayed a relatively slight cytotoxity, which might have a relationship with the exhibited positive potential. PS also showed no appreciate toxicity during the tested concentration (Figure 5B).

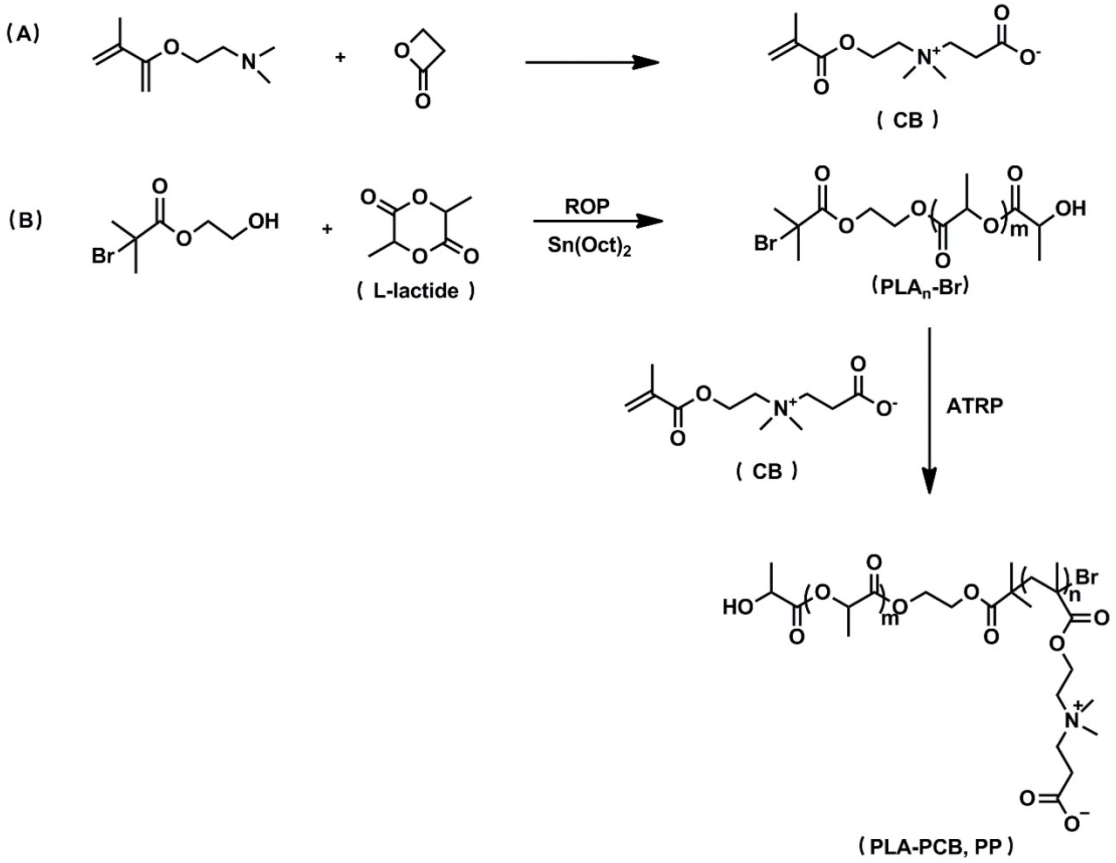


**Figure 2. Synthetic route of biomaterials.** (A) CB monomer. (B) PLA-PCB diblock copolymer.

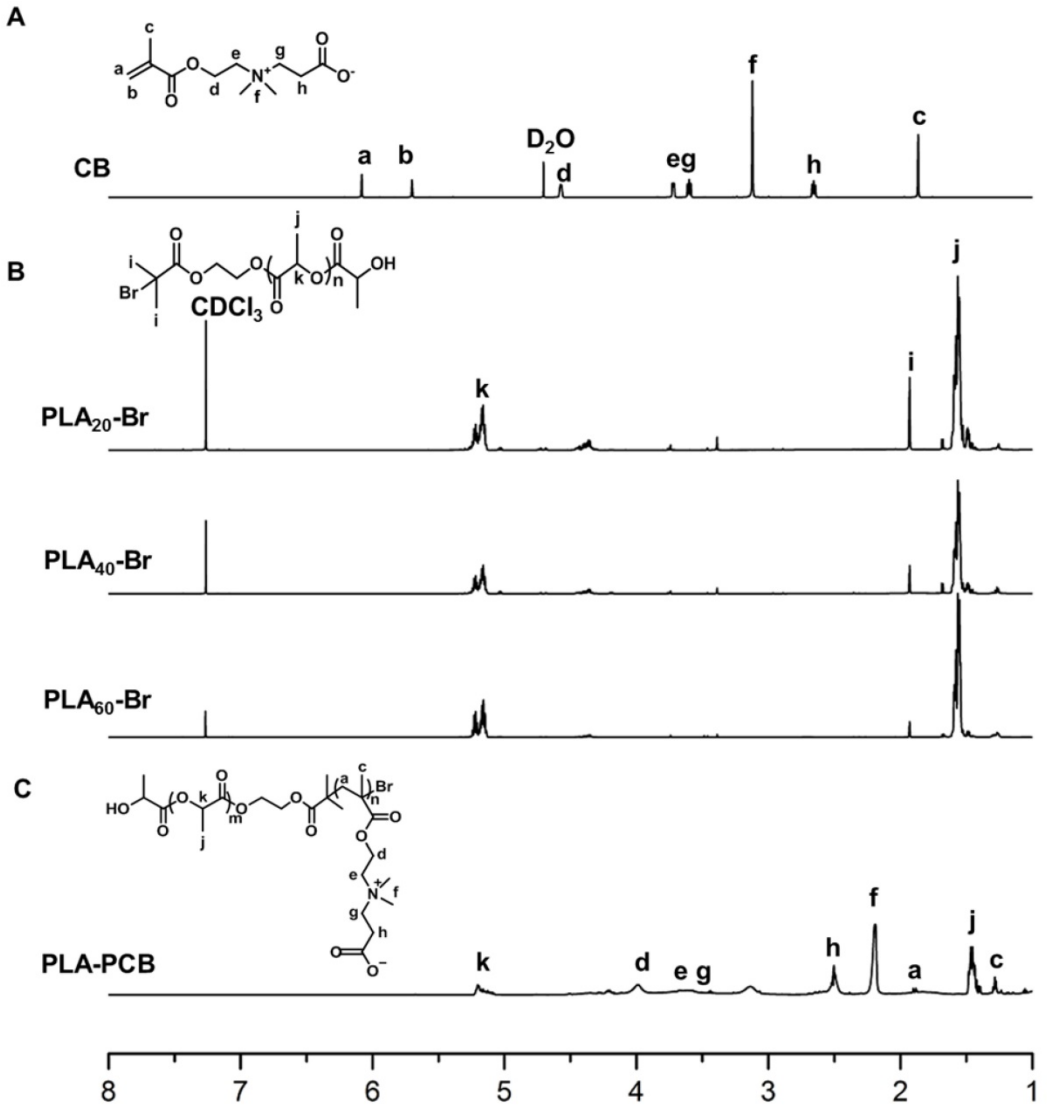


**Figure 3. $^1$H NMR spectra recorded for biomaterials.** (A) Monomer CB. (B) Macroinitiators $PLA_n$-Br of different DPs. (C) Diblock copolymer PLA-PCB (PP).

## Cellular uptake and endosomal/lysosomal escape of PP/PS@MIONs

The cellular uptake of PP/PS@MIONs was confirmed and quantified by using a fluorescence activated cell sorting (FACS) after incubating RAW264.7 macrophages with Cy7-labeled PP/PS@MIONs or PP@MIONs over time. A concentration of 0.10 mg Fe/mL (with PS 0.3 mM) was selected as the maximal nanoparticle concentration with no significant influence on cell viability (Figure 5A). As illustrated in Figure 5C, PP/PS@MIONs showed significantly more internalization than PP@MIONs at 1 h and 2 h. The mean fluorescence intensity (MFI) of the cells containing Cy7-labeled NPs was also measured (Figure 5D). The uptake of Cy7-labeled NPs increased over time. Compared with PP@MIONs, PP/PS@MIONs showed much higher cellular uptake in 12 h and persistently up to 24 h. These were attributed to the specific recognition and phagocytosis of the PS-presenting NPs through the PSR on macrophages. The electrostatic interactions between zwitterionic PCB and the cell membrane might also help the NPs to get close to the macrophages and contribute to the interaction and the engulfment.

After being endocytosed, the NPs needed to escape from endosomes/lysosomes to release the MIONs into the cytoplasm for MRI since the low pH in the lysosomes could break the iron oxide NPs into iron ions [40, 41]. The PP/PS@MIONs and free PS were co-incubated RAW264.7 macrophages (Figure 6). PS were marked blue and the endosomes/lysosomes were stained red. The blue PP/PS@MIONs kept highly co-localization with the red endosomes/lysosomes after 4 h. This meant that most of the NPs were retained in the endosomes/lysosomes. After 12 h, a large proportion

of blue fluorescence of PP/PS@MIONs separated from the red fluorescence of endosomes/lysosomes. This suggested that most of PP/PS@MIONs successfully escaped from endosomes/lysosomes. For PP/PS@MIONs group, the co-localization ratio had a 31.3% decrease, while no significant change was observed for Free-PS group. These results confirmed that the PCB-based NPs were capable of escaping from the endosomes/lysosomes due to the protonation process of PCB under the acid condition. The quick escape also protected the encapsulated MIONs to avoid from degrading into iron ions, and ensured the magnetic properties of PP/PS@MIONs for MRI.

### *In vitro* immunomodulation

Whether the PP/PS@MIONs could mimic apoptotic uptake and elicit modulating and anti-inflammatory functions was very important for the application of this theranostic system. Peritoneal macrophages were used, since they were an accessible cell type comparing to cardiac macrophages and had abundant PSR on their cell surfaces [28]. Firstly, LPS as a stimulus was co-incubated with peritoneal macrophages to establish an *in vitro* inflammatory environment. CD86 was a surface marker of pro-inflammatory macrophages and CD206 was a surface marker of anti-inflammatory macrophages [42, 43]. As shown in Figure 7A and B, after treatment with PP/PS@MIONs, the expression of CD86 was significantly decreased, while the expression of CD206 markedly increase. By comparison, the PP@MIONs group and Free-PS group didn't modulate the state of the macrophages. The control group (LPS only) always kept a high level of CD86 expression.

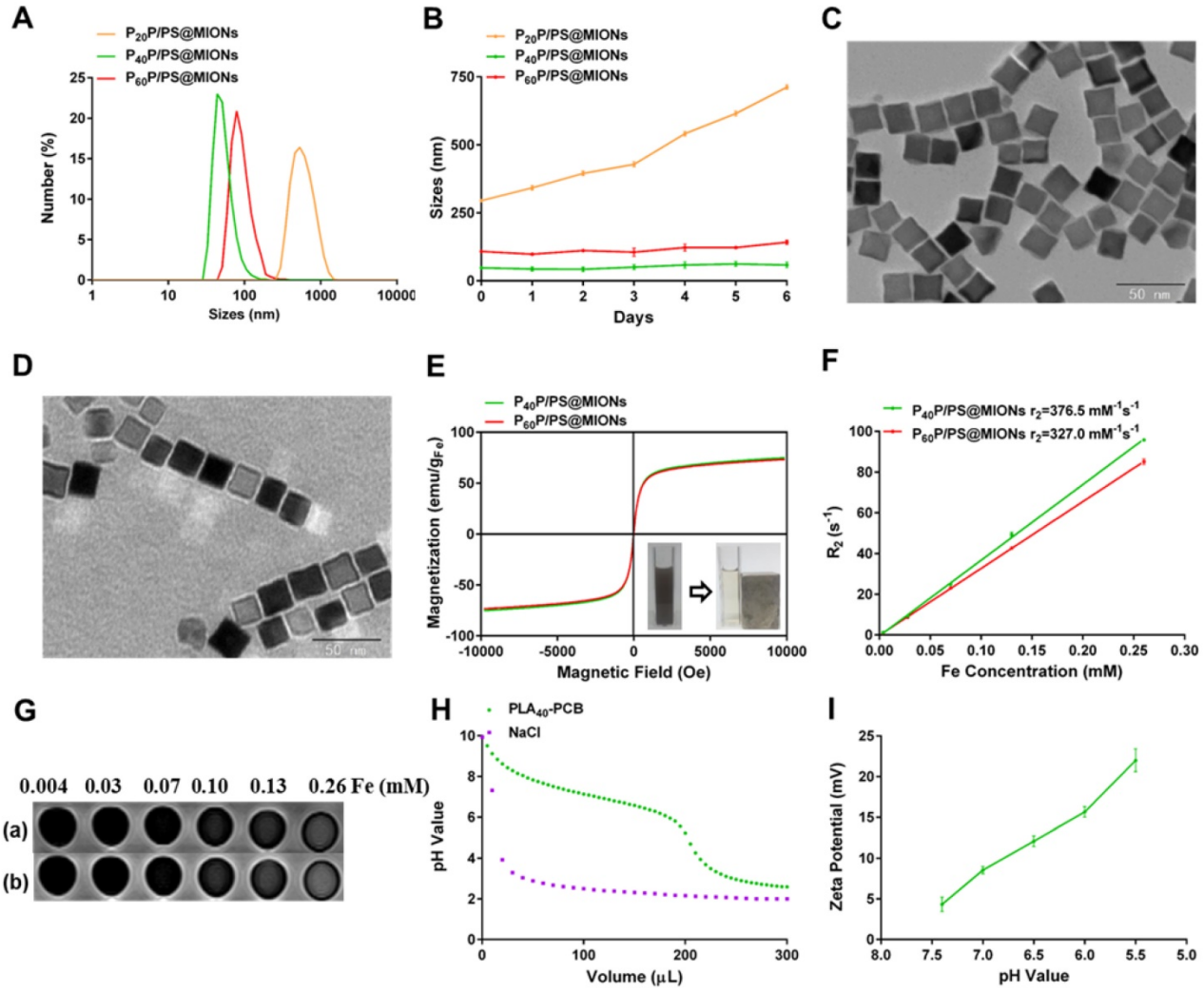


**Figure 4. Characterization of MIONs formulations.** (A) Sizes distribution and (B) stability in PBS with 10% FBS of PP/PS@MIONs. TEM images of (C) MIONs and (D) $P_{40}$P/PS@MIONs. (E) *M-H* curves, (F) $r_2$ relaxivity and (G) MR images of (a) $P_{40}$P/PS@MIONs and (b) $P_{60}$P/PS@MIONs, respectively. Insert picture exhibited the accumulation of $P_{40}$P/PS@MIONs induced by a magnetic field. (H) The buffering capacity of $PLA_{40}$-PCB and (I) pH value dependent zeta potential of $P_{40}$P/PS@MIONs. Data are shown mean ± SD.

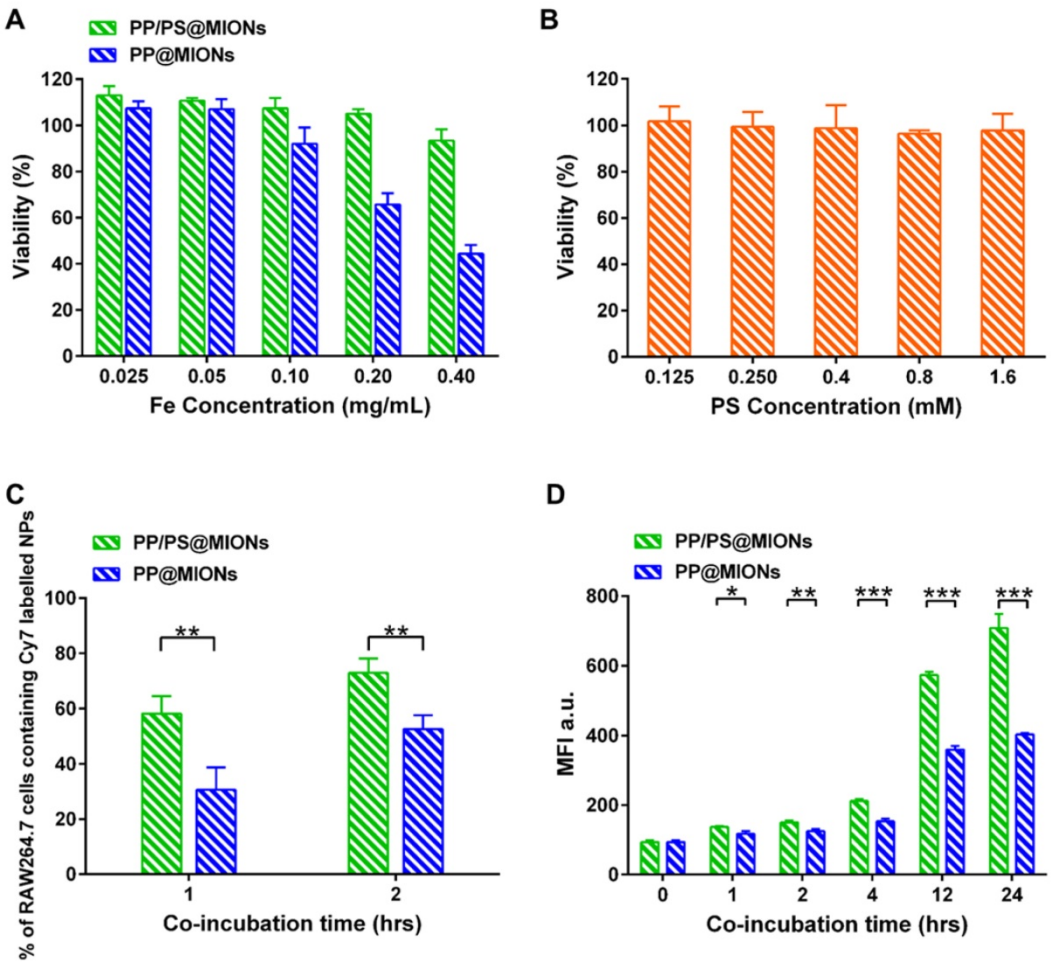


**Figure 5. *In vitro* cytotoxicity and cellular uptake.** *In vitro* cytotoxicity of (A) PP/PS@MIONs, PP@MIONs and (B) PS. (C) Percentage of macrophages containing Cy7-labeled NPs after co-incubation of 1 and 2 hours. (D) Mean fluorescence intensity (MFI) of macrophages containing Cy7-labeled NPs after co-incubation of various periods of time. Data are shown mean ± SD. *: differences between PP/PS@MIONs group and PP@MIONs group, *: $P < 0.05$, **: $P < 0.01$, ***: $P < 0.005$.

Furtherly, the cell supernatant was detected by ELISA tests to determine the levels of the cytokines secretion. TNF-α and IL-1β could be seen as the marker of inflammation, and TGF-β1 and IL-10 were the markers indicating the inflammation resolution [44-48]. In Figure 7C-F, compared to the control group, PP/PS@MIONs group showed significant suppression of TNF-α and IL-1β secretion and high up-regulation of TGF-β1 and IL-10. Whereas, the PP@MIONs and Free-PS groups didn't modulate the levels of the cytokines. The control group always kept high levels of TNF-α and IL-1β indicating an inflammation state. All these findings indicated that PP/PS@MIONs could mimic apoptosis, which led to reprograming of macrophages and an anti-inflammatory response.

## *In vivo* pharmacokinetics

The *in vivo* pharmacokinetics of all the formulations were investigated and calculated by non-compartment pharmacokinetic model. As shown in Figure 8, free PS was quickly removed from the circulating system after intravenous administration, with the plasma half-time ($t_{1/2}$) 1.68 h. The plasma half-time of PP/PS@MIONs labeled by the FA was 15.67 h, which was over 9-fold higher than that of free PS. The PP@MIONs did not contain the PS drug, herein, hydrophobic Cy7 was encapsulated in the MIONs formulations to track the blood concentration of nanoparticles. These two nanoparticles exhibited comparable circulation profiles for *in vivo* study. The long circulation time was due to the encapsulated copolymers PP in the nanoparticles, and was very crucial for the sufficient accumulation in the targeted heart tissues. Besides, the FDA-approved Ferumoxytol was reported to have a blood half-life of 15 h in human. And the blood half-life in humans were frequently longer than these in animals [49]. Hence, the long blood circulation of our nanosystem would be very benefit for future clinical application in MRI of MI.

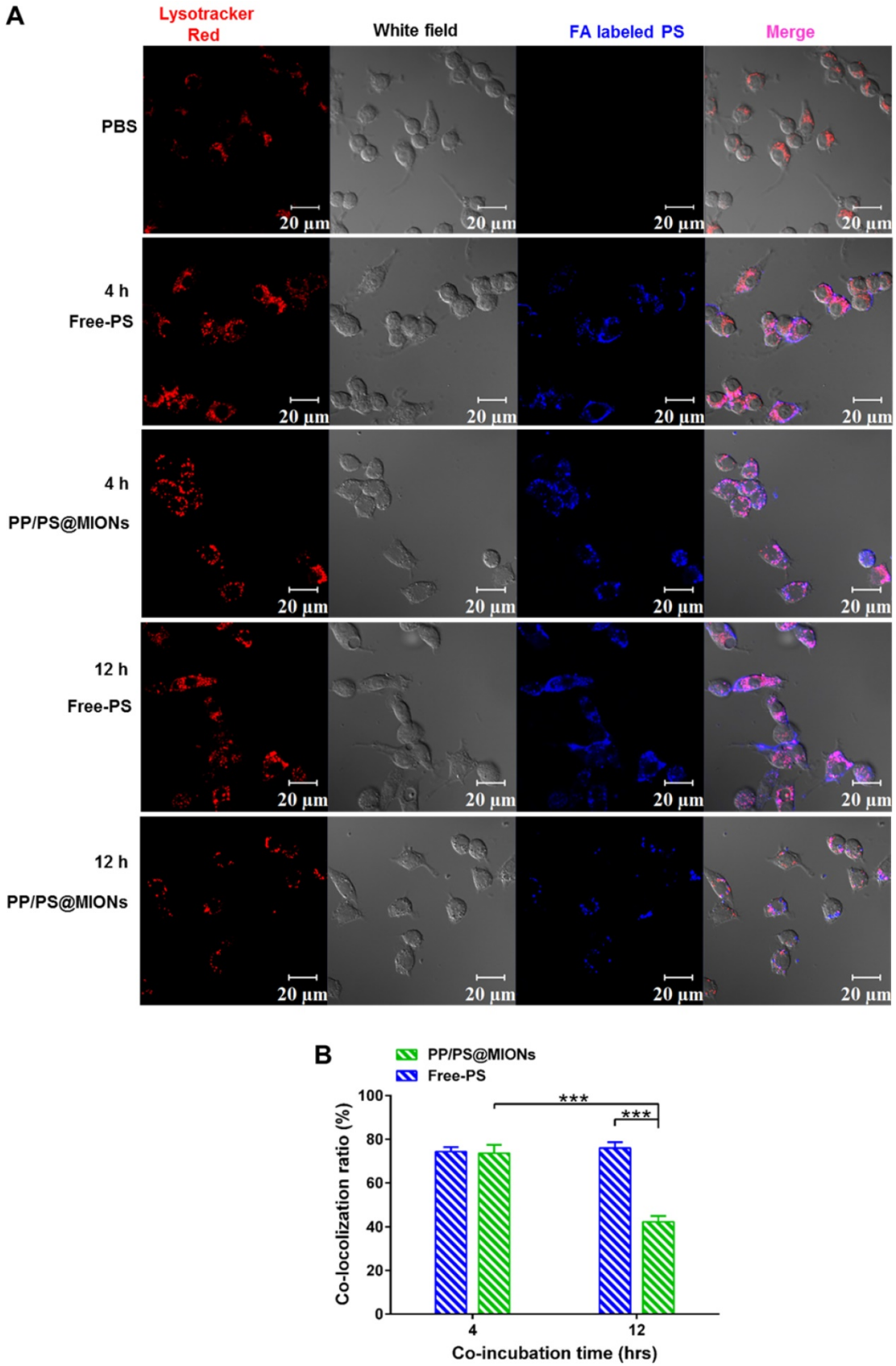


**Figure 6.** ***In vitro*** **cellular uptake and endosomal/lysosomal escape of PP/PS@MIONs.** (A) CLSM images of endosomal/lysosomal escape of NPs in macrophages after 4 h and 12 h of co-incubation. (B) The qualified co-localization ratio of the fluorescence intensity of FA labeled formulations and Lysotracker Red by calculating from 8 random fields of view. Endosomes/lysosomes were stained with Lysotracker Red with an excitation wavelength of 534 nm. PS labeled with FA had a blue fluorescence with an excitation wavelength of 390 nm. Data are shown mean ± SD. *: differences between different groups, *: $P < 0.05$, **: $P < 0.01$, ***: $P < 0.005$.

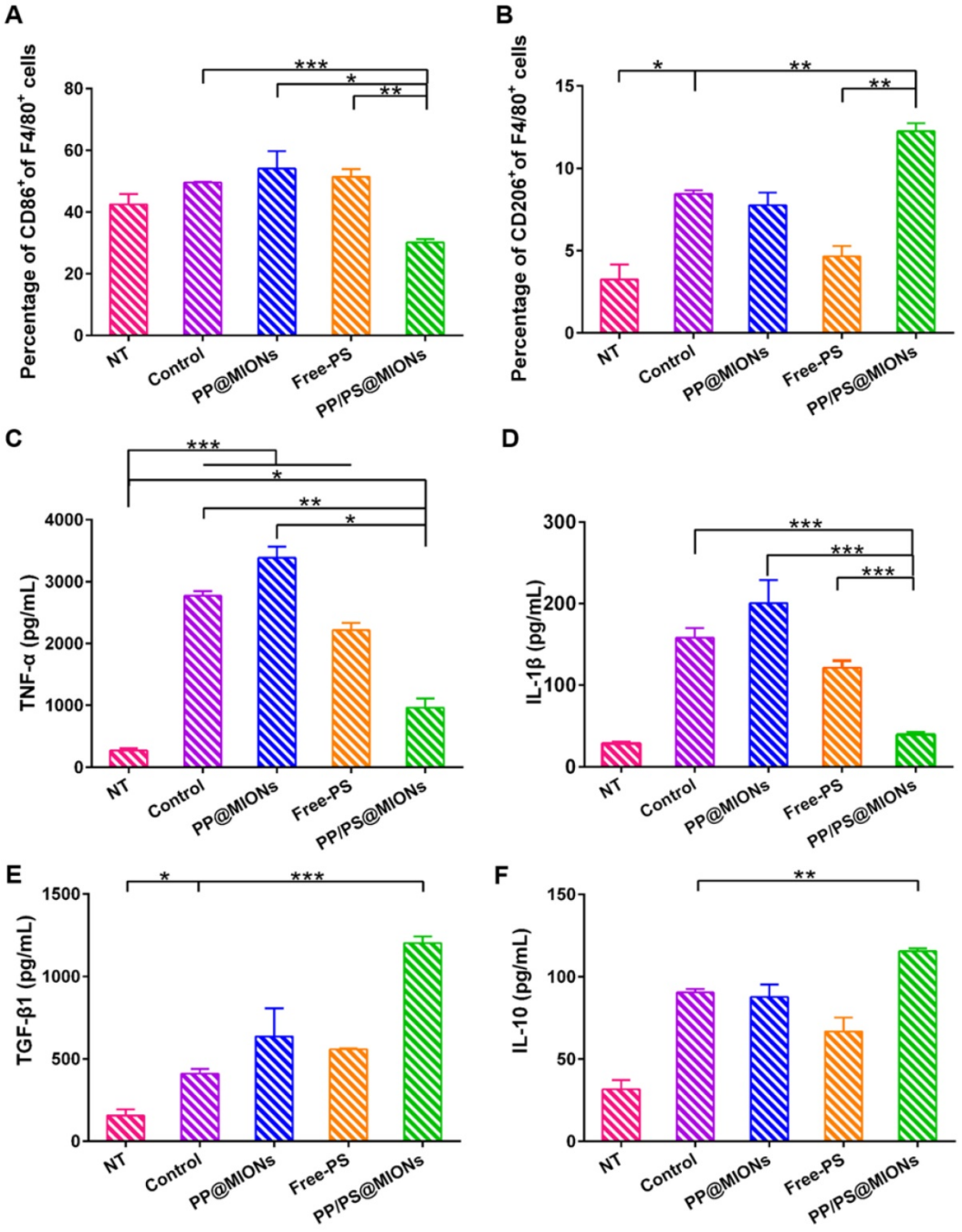


**Figure 7.** ***In vitro*** **immunomodulation of PP/PS@MIONs.** FACS analyzed the relative expression of (A) CD86 and (B) CD206. Release levels of (C) TNF-α, (D) IL-1β, (E) TGF-β1 and (F) IL-10. Data are shown mean ± SD. *: differences between different groups, *: $P < 0.05$, **: $P < 0.01$, ***: $P < 0.005$.

## MR imaging of PP/PS@MIONs *in vivo*

The application of PP/PS@MIONs in MRI for early MI was important for the diagnostic part of the theranostic system. In this study, MI animal model were induced by permanent ligation of anterior descending branch of left coronary artery in rats. The prolonged ischemia and necrosis in infarcted tissue initiated an intense inflammatory response, which could be stained by hematoxylin-eosin (HE) method. As shown in Figure 9A, there were massive infiltrated inflammatory cells (black arrows) in infarcted tissue of MI rats. Remarkable necrosis and degeneration (green circles) also could be seen. By contrast, no abnormal inflammatory phenomenon or injury were observed in sham group. Based on the above results of magnetic properties and cellular uptake, the imaging ability of PP/PS@MIONs of MRI for MI *in vivo* was evaluated (Figure 9B). Rats were injected with NPs by cauda vein with or without an external magnetic field. The saline and PP@MIONs groups exhibited no negative signal enhancement, while the notable

negative signal enhancement (white arrow) could be seen in infarcted area after treated with PP/PS@MION. The results were consistent with the specific accumulation of PP/PS@MIONs. This indicated that PP/PS@MIONs could target to the infarcted area due to the PS targeting. With an external magnetic field, more negative signal enhancement was displayed in infarcted area (white arrow). The enhanced accumulation in infarcted area could be accounted for the presence of magnet. The contrast for MRI induced by PP/PS@MIONs accumulation in the injured area was quantified by assessing the relative signal intensity (Figure 9C). Saline and PP@MIONs groups didn't show any obvious change of signal intensity. However, in the infarcted areas of rats received injection of PP/PS@MIONs, the signal intensity was diminished by 23.62%. While in the presence of an external magnet, the signal intensity significantly decreased by 30.74%. All these data suggested that external magnetic targeting and PS targeting could effectively guide PP/PS@MIONs to the infarcted myocardium, and obviously enhance the accuracy of MR image in MI models. These made the nanosystem PP/PS@MIONs work as an efficient MRI contrast agent for MI at early stage.

To validate the accumulation, cross-sections from the treated hearts were stained with Prussian blue after MRI correspondingly. As displayed in Figure 9D, extremely little blue staining (black arrows) were exhibited in the PP@MIONs group and no staining showed in the saline group. The blue staining increased in the group treated with PP/PS@MIONs, while the most of blue staining were observed in the infarcted myocardium of rats treated with PP/PS@MIONs with the magnet. Also, the concentration of iron was assayed 1 d after intravenous administration of the various MIONs formulation (Figure S1). The highest iron level was shown in the heart of the PP/PS@MIONs treated group. These findings were consisted with the MRI results, and indicated that long circulation and dual targets contributed to improve the accumulation of PP/PS@MIONs in infarcted area.

## Cardiac function *in vivo*

The specific accumulation of PP/PS@MIONs in infarcted tissue and the anti-inflammatory function prompted us to find out if PP/PS@MIONs injected by cauda vein could improve the cardiac function. It had been reported that the number of macrophages in injured area peaked 48 h post MI compared to that immediately post MI [13, 50]. So different formulations were injected 48 h after the MI surgery. Before the NPs injection, cardiac cine was used to test the effects of various formulations on the cardiac function before the injection and again 1 month after the injection. Short-axis MR images were collected and the structure and function parameters, like left ventricle end-diastolic volume (EDV), end-systolic volume (ESV) and ejection fraction (EF) were analyzed. As shown in Figure 10A, B and C, all these indices of cardiac function were negatively altered in rats with MI. Treatment with PP@MIONs or free PS had no effect on the cardiac function of MI rats. Rats treated with PP/PS@MIONs improved EF and preserved the left ventricular dilation. However, PP/PS@MIONs exposed to a magnet treatment preserved EDV, ESV and EF significantly, which indicated that the cardiac function was obviously restored. This might be due to increased accumulation of PP/PS@MIONs by the dual targets.

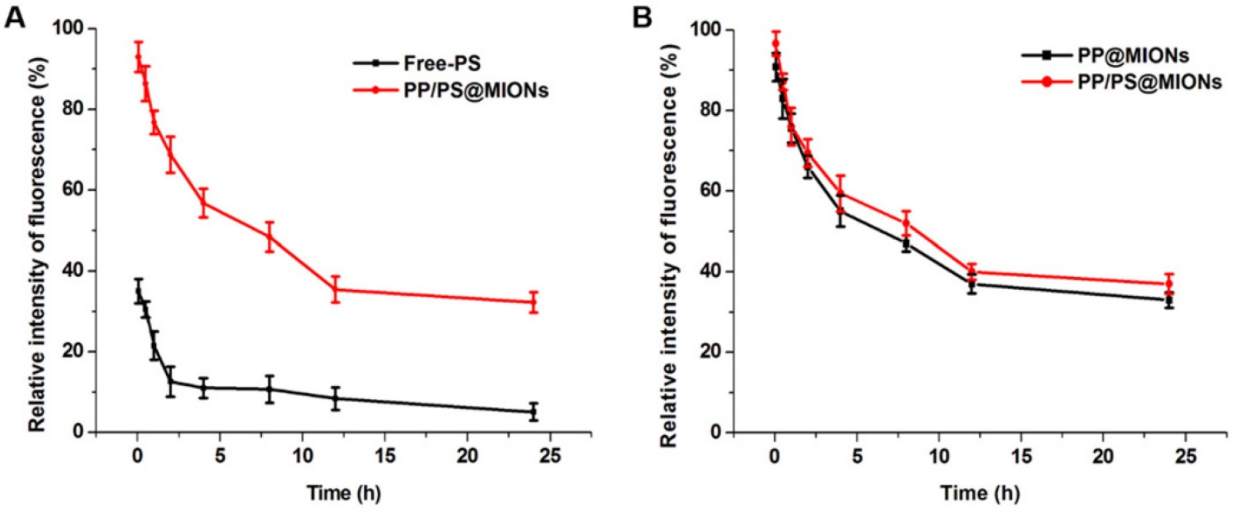


**Figure 8. *In vivo* pharmacokinetics.** The relative intensity fluorescence of fluorescamine (FA) profiles of Free-PS and PP/PS@MIONs (A) labeled by the FA, and the relative intensity fluorescence of Cy7 profiles of PP@MIONs and PP/PS@MIONs (B) marked by the Cy7. Data are Data are shown mean ± SD. of three independent experiments.

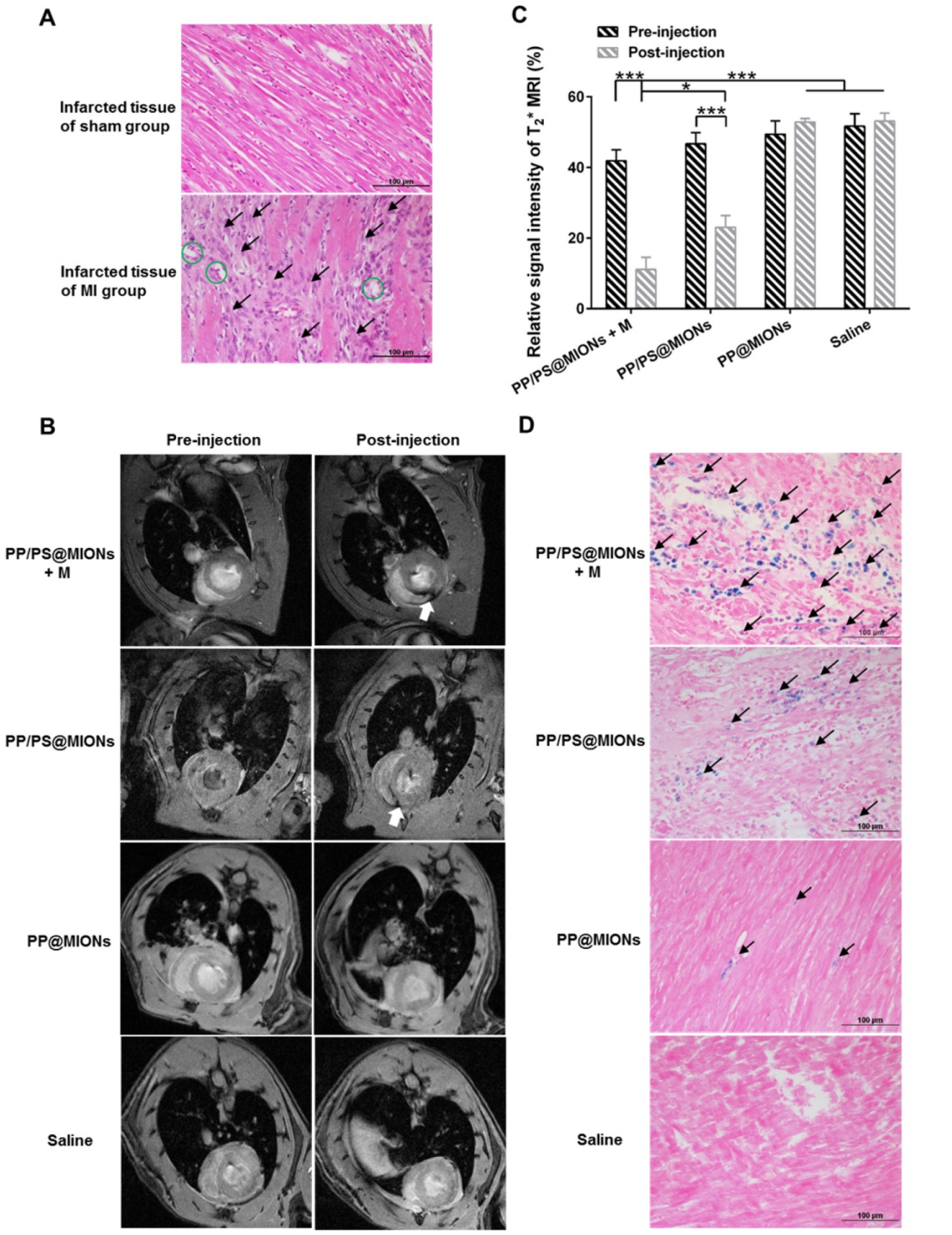


**Figure 9.** ***In vivo*** **MRI of PP/PS@MIONs and cross-sections stained with HE and Prussian blue of hearts.** (A) Photomicrograph of representative HE stain sections from infarcted tissue of MI group and sham group. Black arrows showed the infiltration of inflammatory cells and green circles showed the tissue underwent necrosis and degeneration. (B) Representative MR images of hearts before and 24 h after *i.v.* administration of PP/PS@MIONs and PP@MIONs with or without a magnet. White arrows pointed to the infarcted area. (C) The quantified relative signal intensity of the hearts. (D) Prussian blue staining of the infarcted area of different groups after MRI. Black arrows pointed to blue stained iron. M: magnet. Data are shown mean ± SD. *: differences between different groups, *: $P < 0.05$, **: $P < 0.01$, ***: $P < 0.005$.

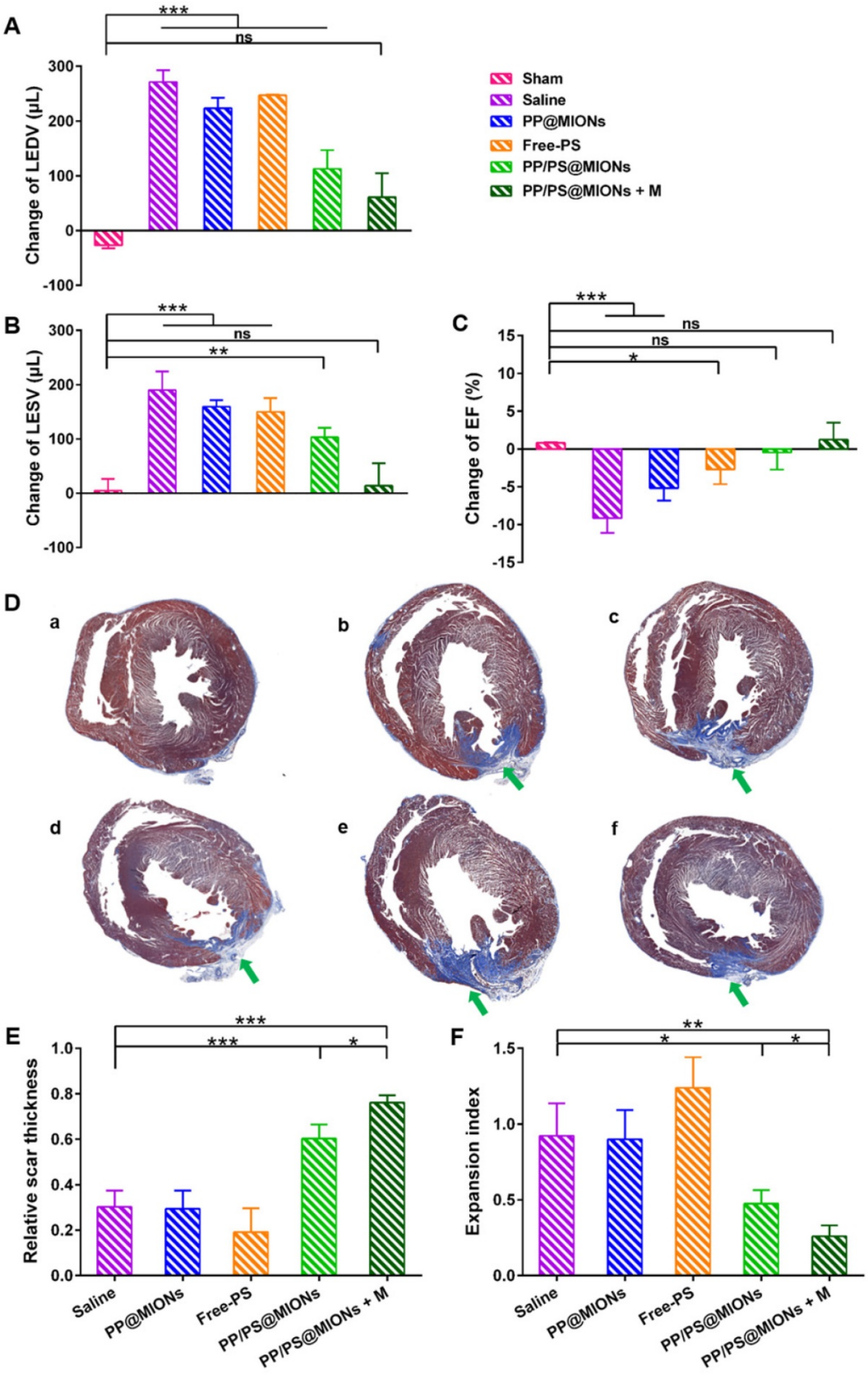


**Figure 10. Effects of PP/PS@MIONs on cardiac function post MI.** Change of (A) EDV, (B) ESV and (C) EF of LV. (D) Images of Masson's tri-chrome-stained sections of infarcted area 1 month after treatment. Blue area showed the infarcted scar (green arrows). The image (a) to (f) are representative image of groups of the sham, saline, PP@MIONs, Free-PS, PP/PS@MIONs and PP/PS@MIONs with a magnet, respectively. (E) The relative scar thickness of the hearts was calculated as average scar thickness divided by average wall thickness. (F) The expansion index of the hearts was calculated as follows: (LV cavity area/ whole LV area)/ relative scar thickness. M: magnet. LV: left ventricular, EDV: end-diastolic volume, ESV: end-systolic volume, EF: ejection fraction. Data are shown mean ± SD. *: differences between different groups, *: $P < 0.05$, **: $P < 0.01$, ***: $P < 0.005$, ns: no significance.

Infarct size was a critical parameter of the cardiac function [17]. The infarct sizes of different groups were also examined by the immunohistochemical and morphometric analysis. Masson's trichrome stained cross sections confirmed the smaller relative scars thickness and infarct sizes (blue area, green arrows) in rats treated with PP/PS@MIONs with an external magnet field (Figure 10D). Four parameters were measured to analyze the morphometry of the hearts: average scar thickness, average wall thickness, LV cavity area and whole LV area. To quantify the scar thickness, average scar thickness was divided by average wall thickness to gain the relative scar thickness. And the expansion index, indicating the extent of LV dilation, could be calculated as: (LV cavity area/whole LV area)/relative scar thickness. As shown in Figure 10E and F, the intravenous administration of PP/PS@MIONs could preserve the infarct size obviously. With an external magnet field, the treatment of PP/PS@MIONs could more significantly diminish the infarct size illustrated by relative scar thickness (2.5-fold higher than saline group) and expansion index (3-fold lower than saline group). All these findings confirmed that the theranostic system PP/PS@MIONs could obviously improve the extent of infarct size and LV remodeling induced by MI. They were in corroboration with the anti-inflammatory response elicited by the reparative function of M2 macrophages, which were mediated by the interactions between PS-presenting PP/PS@MIONs and PSR.

MI has been clarified by the cause of an occlusion of the coronary artery and activated an intense inflammation. The unbridled inflammation with high level of pro-inflammatory cytokines would exacerbate the death of myocytes and the damage of the tissue. So the revascularization and recovery of blood flow were vital to reflect the therapeutic effect of the infarcted tissue. To examine the blood flow restoration and the situation of revascularization, 1 month after the injection, flow velocity and spatial vascular profile in the infarcted area were evaluated by LASCA. As shown in Figure 11, the blood flow was seriously impeded for hearts with MI. Compared to saline treatment, PP@MIONs and free PS have no effect on the revascularization. PP/PS@MIONs with a magnet or without could enhance the blood flow, and the result exhibited more distinct in the presence of an external magnetic field. The findings also consisted with the results above and suggested that PP/PS@MIONs could enhance the blood flow recovery and revascularization with an external magnetic field.

The biocompatibility of PP/PS@MIONs was very crucial for the *in vivo* application. Hence, the biodistribution of various MIONs formulations was evaluated in hearts and normal organs after 1 month (Figure S1), and the Prussian blue staining of the tissues was also demonstrated (Figure S2). As illustrated, the concentration of iron in these organs was almost similar with that of the saline control group. These meant that the iron oxide nanocube in the PP/PS@MIONs might have already been degraded. And the tissues, including hearts, did not shown any obvious staining after 1 month post administration. As it was reported the iron oxide nanoparticles could be eventually degraded and metabolized by the reticuloendothelial system, including the liver and spleen [7, 11]. Considering the iron biodistribution at 1 d and 1 month, the PP/PS@MIONs could be effectively cleared from the liver, spleen and kidney. Moreover, the morphology of the tissues was similar with the saline group, which did not exhibit any toxicity to the normal tissues. These data demonstrated that our theranostic system could be used as safe and effective MRI contrast agents and inflammation-resolving agents for MI at early stage.

## Conclusion

In summary, by mimicking apoptosis, dual-targeting theranostic system PP/PS@MIONs was constructed to realize diagnosis and therapy simultaneously at early stage of MI. With magnetic field and PS targeting, PP/PS@MIONs could significantly enhanced the accumulation in the infarcted area. Through mimicking the apoptotic cells, PS in the theranostic system was largely targeted to PSR on surface of macrophages to mediate the engulfment, which could regulate the macrophages to reparative M2 phenotype and elicit an anti-inflammatory response. This helped to preserve the left ventricular remodeling and obviously improve the cardiac function. On the other hand, after endocytosis, protonated PCB could facilitate the endosomal/lysosomal escape of MIONs, which contributed to the enhanced accumulation of MIONs in the cytoplasm. PP/PS@MIONs could sharply decrease the signal intensity in $T_2$* MRI and realize accurate and high sensitivity imaging of MI. Hence, the long circulation and high biocompatibility made PP/PS@MIONs be used as a safe and promising contrast agent to assess MI at early stage *via* the detection of macrophages. Moreover, by mimicking apoptosis, external magnetic field induced PP/PS@MIONs could realize accurate diagnosis and site-specific treatment of the inflammatory stage in Lewis rats of MI model. This provides a viable and potential theranostic system for MI clinical application in the future.

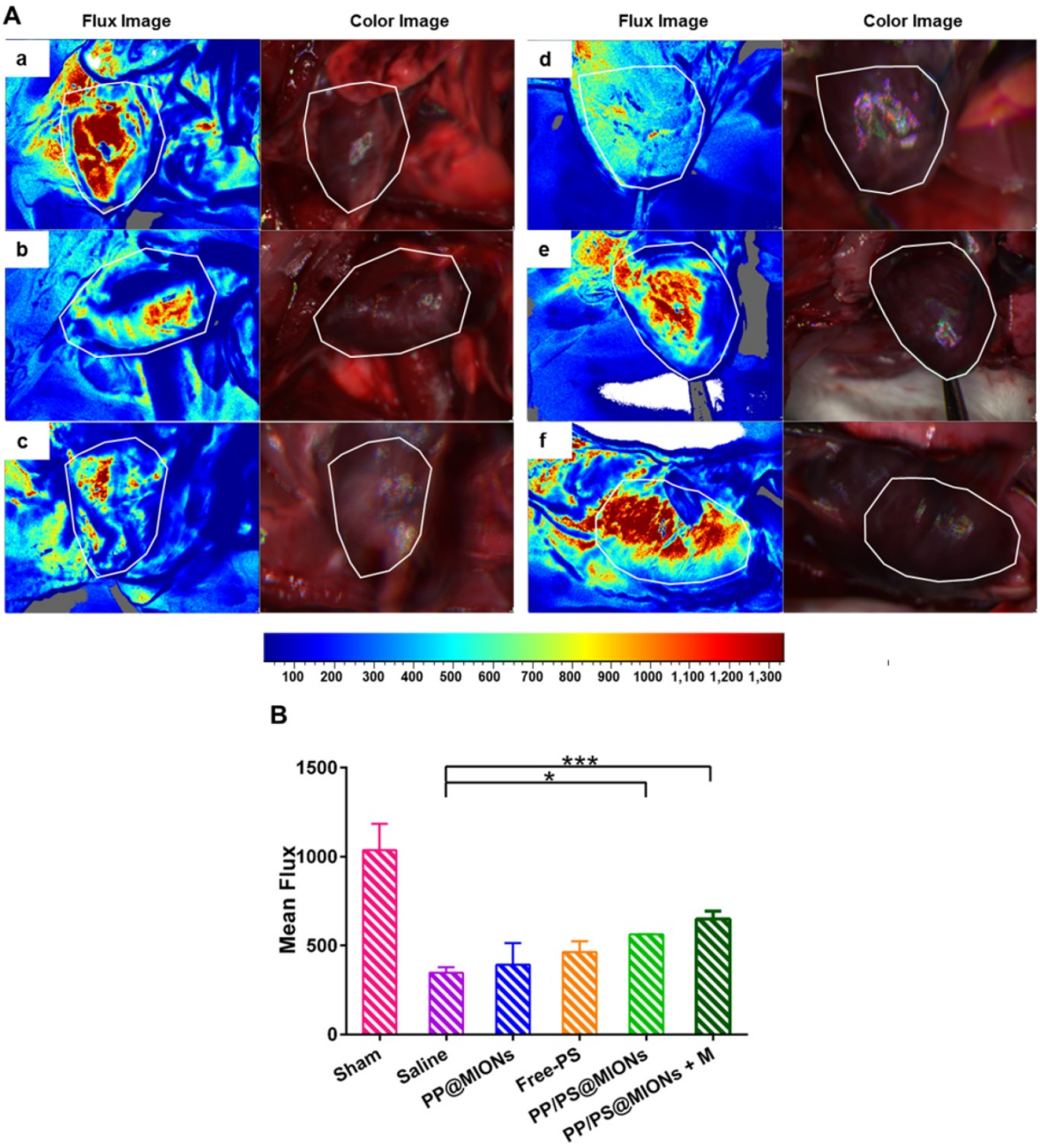


**Figure 11. Results of Blood flow restoration.** (A) Flow velocity and spatial vascular profile in the infarcted area of different groups were evaluated by LASCA. The image (a) to (f) are representative image of groups of the sham, saline, PP@MIONs, Free-PS, PP/PS@MIONs and PP/PS@MIONs with a magnet, respectively. M: magnet. White polygons showed the regions of interest. (B) The mean flux was qualified. Data are shown mean ± SD. *: differences between different groups, *: $P < 0.05$, **: $P < 0.01$, ***: $P < 0.005$.

## Supplementary Material

Supplementary figures.
http://www.thno.org/v07p4149s1.pdf

## Acknowledgments

This work was financially supported by the National High Technology Research and Development Program (2016YFA0200303), the National Natural Science Foundation of China (51573188, 51373177, 31522023), Beijing Municipal Science & Technology Commission No. Z161100002616015 and the "Strategic Priority Research Program" of the Chinese Academy of Sciences (XDA09030301-3).

## Competing Interests

The authors have declared that no competing interest exists.

# References


1. Mendis S, Puska P, Norrving B. Global Atlas on cardiovascular disease prevention and control. Geneva Workd Health Organization; 2011.
2. Konstam MA, Kramer DG, Patel AR, Maron MS, Udelson JE. Left ventricular remodeling in heart failure: current concepts in clinical significance and assessment. JACC Cardiovasc Imaging. 2011; 4: 98-108.
3. Epelman S, Liu PP, Mann DL. Role of innate and adaptive immune mechanisms in cardiac injury and repair. Nat Rev Immunol. 2015; 15: 117-29.
4. Frangogiannis NG. The inflammatory response in myocardial injury, repair, and remodelling. Nat Rev Cardiol. 2014; 11: 255-65.
5. Opie LH, Commerford PJ, Gersh BJ, Pfeffer MA. Controversies in ventricular remodelling. Lancet. 2006; 367: 356-67.
6. Frantz S, Nahrendorf M. Cardiac macrophages and their role in ischaemic heart disease. Cardiovasc Res. 2014; 102: 240-8.
7. Weissleder R, Nahrendorf M, Pittet MJ. Imaging macrophages with nanoparticles. Nat Mater. 2014; 13: 125-38.
8. Velagaleti RS, Pencina MJ, Murabito JM, Wang TJ, Parikh NI, D'Agostino RB, et al. Long-term trends in the incidence of heart failure after myocardial infarction. Circulation. 2008; 118: 2057-62.
9. Pfeffer MA, Braunwald E, Moyé LA, Basta L, Edward J. Brown J, Cuddy TE, et al. Effect of captopril on mortality and morbidity in patients with left ventricular dysfunction after myocardial infarction. Results of the survival and ventricular enlargement trial. The SAVE Investigators. N Engl J Med. 1992; 327: 669-77.
10. Sosnovik DE, Nahrendorf M, Weissleder R. Magnetic nanoparticles for MR imaging: agents, techniques and cardiovascular applications. Basic Res Cardiol. 2008; 103: 122-30.
11. Finn JP, Nguyen K-L, Han F, Zhou Z, Salusky I, Ayad I, et al. Cardiovascular MRI with ferumoxytol. Clin Radiol. 2016; 71: 796-806.
12. Kempf T, Zarbock A, Vestweber D, Wollert KC. Anti-inflammatory mechanisms and therapeutic opportunities in myocardial infarct healing. J Mol Med (Berl). 2012; 90: 361-9.
13. Nahrendorf M, Pittet MJ, Swirski FK. Monocytes: protagonists of infarct inflammation and repair after myocardial infarction. Circulation. 2010; 121: 2437-45.
14. Somasuntharam I, Yehl K, Carroll SL, Maxwell JT, Martinez MD, Che P-L, et al. Knockdown of TNF-α by DNAzyme gold nanoparticles as an anti-inflammatory therapy for myocardial infarction. Biomaterials. 2016; 83: 12-22.
15. Timmers L, Lim SK, Hoefer IE, Arslan F, Lai RC, Oorschot AAMv, et al. Human mesenchymal stem cell-conditioned medium improves cardiac function following myocardial infarction. Stem Cell Res. 2011; 6: 206-14.
16. Dobaczewski M, Xia Y, Bujak M, Gonzalez-Quesada C, Frangogiannis NG. CCR5 Signaling suppresses inflammation and reduces adverse remodeling of the infarcted heart, mediating recruitment of regulatory T cells. Am J Pathol. 2010; 176: 2177-87.
17. Cuadrado I, Piedras MJGM, Herruzo I, Turpin MdC, Castejón B, Reventun P, et al. EMMPRIN-targeted magnetic nanoparticles for in vivo visualization and regression of acute myocardial infarction. Theranostics. 2016; 6: 545-57.
18. Montet-Abou K, Daire J-L, Hyacinthe J-N, Jorge-Costa M, Grosdemange K, Mach F, et al. In vivo labelling of resting monocytes in the reticuloendothelial system with fluorescent iron oxide nanoparticles prior to injury reveals that they are mobilized to infarcted myocardium. Eur Heart J. 2010; 31: 1410-20.
19. Alam SR, Shah ASV, Richards J, Lang NN, Barnes G, Joshi N, et al. Ultrasmall superparamagnetic particles of iron oxide in patients with acute myocardial infarction: early clinical experience. Circ Cardiovasc Imaging. 2012; 5: 559-65.
20. Yilmaz A, Dengler MA, Kuip Hvd, Yildiz H, Rösch S, Klumpp S, et al. Imaging of myocardial infarction using ultrasmall superparamagnetic iron oxide nanoparticles: a human study using a multi-parametric cardiovascular magnetic resonance imaging approach. Eur Heart J. 2013; 34: 462-75.
21. Li MO, Sarkisian MR, Mehal WZ, Rakic P, Flavell RA. Phosphatidylserine receptor is required for clearance of apoptotic cells. Science. 2003; 302: 1560-3.
22. Ravichandran KS, Lorenz U. Engulfment of apoptotic cells: signals for a good meal. Nat Rev Immunol. 2007; 7: 964-74.
23. Wu Y, Tibrewal N, Birge RB. Phosphatidylserine recognition by phagocytes: a view to a kill. Trends Cell Biol. 2006; 16: 189-97.
24. Kalden JR, Herrmann M. Anti-inflammatory and immunoregulatory effects of apoptotic cells. Apoptosis and Autoimmunity: Wiley - VCH Verlag GmbH & Co. KGaA; 2004:37-56.
25. Cvetanovic M, Ucker DS. Innate immune discrimination of apoptotic cells: repression of proinflammatory macrophage transcription is coupled directly to specific recognition. J Immunol. 2004; 172: 880-9.
26. Fadok VA, Voelker DR, Campbell PA, Cohen JJ, Bratton DL, Henson PM. Exposure of phosphatidylserine on the surface of apoptotic lymphocytes triggers specific recognition and removal by macrophages. J Immunol. 1992; 148: 2207-16.
27. Savill J, Gregory C. Apoptotic PS to phagocyte TIM-4: eat me. Immunity. 2007; 27: 830-2.
28. Kobayashi N, Karisola P, Peña-Cruz V, Dorfman DM, Jinushi M, Umetsu SE, et al. TIM-1 and TIM-4 glycoproteins bind phosphatidylserine and mediate uptake of apoptotic cells. Immunity. 2007; 27: 927-40.
29. Fadok VA, Bratton DL, Rose DM, Pearson A, Ezekewitz RAB, Henson PM. A receptor for phosphatidylserine-specific clearance of apoptotic cells. Nature. 2000; 405: 85-90.
30. Kim D, Lee N, Park M, Kim BH, An K, Hyeon T. Synthesis of uniform ferrimagnetic magnetite nanocubes. J Am Chem Soc. 2009; 131: 454-5.
31. Li Y, Liu R, Yang J, Ma G, Zhang Z, Zhang X. Dual sensitive and temporally controlled camptothecin prodrug liposomes codelivery of siRNA for high efficiency tumor therapy. Biomaterials. 2014; 35: 9731-45.
32. Qiao C, Liu J, Yang J, Li Y, Weng J, Shao Y, et al. Enhanced non-inflammasome mediated immune responses by mannosylated zwitterionic-based cationic liposomes for HIV DNA vaccines. Biomaterials. 2016; 85: 1-17.
33. Nahire R, Haldar MK, Paul S, Ambre AH, Meghnani V, Layek B, et al. Multifunctional polymersomes for cytosolic delivery of gemcitabine and doxorubicin to cancer cells. Biomaterials. 2014; 35: 6482-97.
34. Green TR, Fisher J, Stone M, Wroblewski BM, Ingham E. Polyethylene particles of a 'critical size' are necessary for the induction of cytokines by macrophages in vitro. Biomaterials. 1998; 19: 2297-302.
35. Wang G-W, Guo Y, Vondriska TM, Zhang J, Zhang S, Tsai LL, et al. Acrolein consumption exacerbates myocardial ischemic injury and blocks nitric oxide-induced PKCε signaling and cardioprotection. J Mol Cell Cardiol. 2008; 44: 1016-22.
36. Franco F, Thomas GD, Giroir B, Bryant D, Bullock MC, Chwialkowski MC, et al. Magnetic resonance imaging and invasive evaluation of development of heart failure in transgenic mice with myocardial expression of tumor necrosis factor-alpha. Circulation. 1999; 99: 448-54.
37. Alhaddad IA, Tkaczevski L, Siddiqui F, Mir R, Brown EJ. Aspirin enhances the benefits of late reperfusion on infarct shape: a possible mechanism of the beneficial effects of aspirin on survival after acute myocardial infarction. Circulation. 1995; 91: 2819-23.
38. Lee N, Choi Y, Lee Y, Park M, Moon WK, Choi SH, et al. Water-dispersible ferrimagnetic iron oxide nanocubes with extremely high $r_2$ relaxivity for highly sensitive in vivo MRI of tumors. Nano Lett. 2012; 12: 3127-31.
39. Zhang R, Li Y, Hu B, Lu Z, Zhang J, Zhang X. Traceable nanoparticle delivery of small interfering RNA and retinoic acid with temporally release ability to control neural stem cell differentiation for alzheimer's disease therapy. Adv Mater. 2016; 28: 6345-52.
40. Thorek DLJ, Chen AK, Czupryna J, Tsourkas A. Superparamagnetic Iron Oxide Nanoparticle Probes for Molecular Imaging. Ann Biomed Eng. 2006; 34: 23-38.
41. Florian A, Ludwig A, Rösch S, Yildiz H, Klumpp S, Sechtem U, et al. Positive effect of intravenous iron-oxide administration on left ventricular remodelling in patients with acute ST-elevation myocardial infarction - a cardiovascular magnetic resonance (CMR) study. Int J Cardiol. 2014; 173: 184-9.
42. Besnard A-G, Guabiraba R, Niedbala W, Palomo J, Reverchon F, Shaw TN, et al. IL-33-mediated protection against experimental cerebral malaria is linked to induction of type 2 innate lymphoid cells, M2 macrophages and regulatory T cells. PLoS Pathog. 2015; 11: e1004607.
43. Stouch AN, Zaynagetdinov R, Barham WJ, Stinnett AM, Slaughter JC, Yull FE, et al. IκB kinase activity drives fetal lung macrophage maturation along a non-M1/M2 paradigm. J Immunol. 2014; 193: 1184-93.
44. Hedayat M, Mahmoudi MJ, Rose NR, Rezaei N. Proinflammatory cytokines in heart failure: double-edged swords. Heart Fail Rev. 2010; 15: 543-62.
45. Kleinbongard P, Schulz R, Heusch G. TNFα in myocardial ischemia/reperfusion, remodeling and heart failure. Heart Fail Rev. 2011; 16: 49-69.
46. Gong K, Chen Y-F, Li P, Lucas JA, Hage FG, Yang Q, et al. Transforming growth factor-β inhibits myocardial PPARγ expression in pressure overload-induced cardiac fibrosis and remodeling in mice. J Hypertens. 2011; 29: 1810-9.
47. Bujak M, Frangogiannis NG. The role of TGF-beta signaling in myocardial infarction and cardiac remodeling. Cardiovasc Res. 2007; 74: 184-95.
48. Miyasato SK, Loeffler J, Shohet R, Zhang J, Lindsey M, Saux CJL. Caveolin-1 modulates TGF-β1 signaling in cardiac remodeling. Matrix Biol. 2011; 30: 318-29.
49. Sosnovik DE, Nahrendorf M. Cells and iron oxide nanoparticles on the move: magnetic resonance imaging of monocyte homing and myocardial inflammation in patients with ST-elevation myocardial infarction. Circ Cardiovasc Imaging. 2012; 5: 551-4.
50. Shi C, Pamer EG. Monocyte recruitment during infection and inflammation. Nat Rev Immunol. 2011; 11: 762-74.